

# Integrated Lithium Niobate Electro-optic Modulators Operating at CMOS-compatible Voltages

Cheng Wang,<sup>1,\*</sup> Mian Zhang,<sup>1,\*</sup> Xi Chen,<sup>2</sup> Maxime Bertrand,<sup>1,3</sup> Amirhassan Shams-Ansari,<sup>1,4</sup> Sethumadhavan Chandrasekhar,<sup>2</sup> Peter Winzer,<sup>2</sup> and Marko Loncar<sup>1,†</sup>

<sup>1</sup>*John A. Paulson School of Engineering and Applied Sciences,  
Harvard University, Cambridge, Massachusetts 02138, USA*

<sup>2</sup>*Nokia Bell Labs, Holmdel, New Jersey 07733, USA*

<sup>3</sup>*LP2N, Institut d'Optique Graduate School, CNRS,  
University of Bordeaux, F-33400, Talence, France*

<sup>4</sup>*Department of Electrical Engineering and Computer Science,  
Howard University, Washington DC 20059, USA*

(Dated: April 15, 2018)

Future communication systems require chip-scale electro-optic modulators that simultaneously operate at low voltages and ultra-high bandwidths, and have low optical insertion losses. Current on-chip modulators have the potential to address this urgent demand, but often come with performance trade-offs due to the use of non-ideal materials. We present a monolithically integrated lithium-niobate electro-optic modulator that simultaneously features a CMOS-level half-wave voltage of 1.4 V and supports ultra-high-speed data transmission at 210 Gigabits per second. Our integrated electro-optic platform breaks the trade-off paradigm of existing active photonic circuits and could provide a practical solution for future ultra-high-performance optoelectronic engines, where photonic components are directly integrated with CMOS circuitry.

High-performance electro-optic modulators, which translate high-speed electronic signals into the optical domain, are critical components of modern fiber networks ranging from trans-Atlantic communication channels to links within a data center [1, 2]. They are also widely used in microwave photonics applications for transmitting and processing analog microwave signals with high fidelity [3, 4]. Furthermore, ultra-fast electro-optic switches and routers are essential for emerging applications in quantum photonics [5, 6], and non-reciprocal optics [7, 8]. These modern optoelectronic applications require ideal modulators that simultaneously feature a low drive voltage, a large bandwidth, a low optical insertion loss, a high extinction ratio, excellent signal quality, and compatibility with large-scale manufacturing. For decades, lithium niobate (LN,  $\text{LiNbO}_3$ ) electro-optic modulators have been the workhorse of the optoelectronic industry due to their excellent signal fidelity and good temperature stability. However, the lack of integrability in LN results in discrete and expensive components that have limited bandwidths ( $\sim 35$  GHz) and require large operating voltages ( $\sim 3.5$  V) [9]. To address the integrability issue, many photonic platforms compatible with microfabrication processes have been pursued, including those based on silicon (Si) [1, 10, 11], indium phosphide (InP) [12, 13], polymers [14, 15] and plasmonics [16]. These platforms have shown excellent scalability and distinct performance merits, including the potential to integrate with CMOS electronics (Si), low driving voltage (InP, polymer), ultrahigh bandwidth (polymer, plasmonics) and small footprint (Si, plasmonics). However, due to the material limitations, an all-around performance that is critically demanded has not been achieved up to this point.

The strong electro-optic (Pockels) effect in LN, which

changes the refractive index linearly upon an applied voltage at femtosecond time scales, in principle allows for ultra-fast modulation, low-voltage operation and low optical loss at the same time [17]. Although it has been known for some time that microstructured LN devices can provide better modulator performance [18], most commercial LN modulators to-date still use titanium indiffusion or proton exchange to create waveguides because of the notoriously difficult dry etching of LN [9]. These waveguides typically have a low refractive index contrast  $\Delta n$  of  $\sim 0.02$  between core and cladding, resulting in a large optical mode size [19]. The weak optical confinement requires metal electrodes to be spaced far apart, significantly lowering the electro-optic efficiency. In recent years, the LN-on-insulator (LNOI) platform has emerged as a promising candidate to fully exploit LNs excellent material properties. In this approach, a single-crystal sub-micron LN thin film is bonded on top of a low-index substrate (i.e. silicon dioxide,  $\text{SiO}_2$ ), and waveguides can be realized by etching the LN device layer [20]. This has resulted in a range of LN photonic devices with high index contrast of  $\sim 0.7$  and tightly-confined optical modes [21–27]. In particular, electro-optic modulators with voltage-length products ( $V_\pi \cdot L$ ) as low as 1.8 V-cm and 3-dB bandwidths up to 40 GHz have been demonstrated [23, 24, 27]. However, the drive voltage and bandwidth in these demonstrations still face critical trade-offs due to non-ideal etching and/or field overlaps. Whether it is possible to simultaneously achieve low half-wave voltage (on/off switching voltage,  $V_\pi$ ), ultra-high bandwidth and low optical loss in LN modulators has remained an outstanding question.

Here we demonstrate monolithically integrated LN electro-optic modulators that break the existing trade-off paradigm and show a  $V_\pi$  of 1.4 V, compatible with

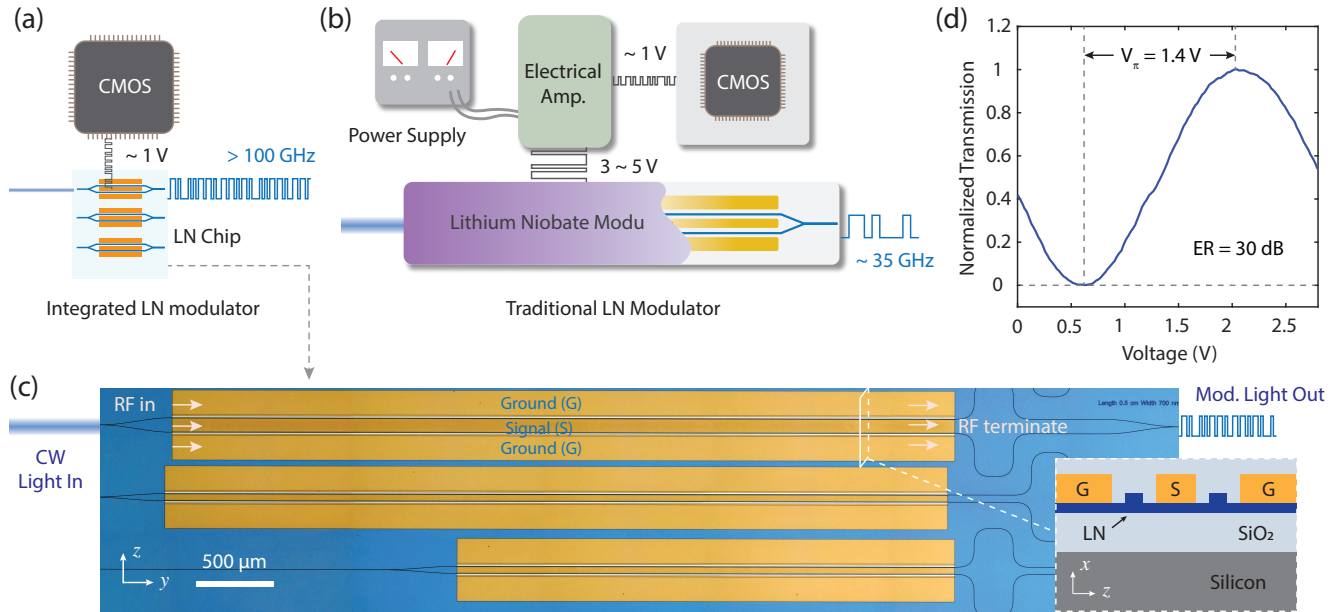


FIG. 1. **Nanophotonic lithium-niobate modulators compatible with CMOS drive voltages.** (a-b) Schematic comparison of the data transmitting setups for integrated (a) and traditional (b) LN modulators. The nanophotonic lithium-niobate modulator supports direct CMOS driving with high bandwidths ( $> 100$  GHz) (a), while traditional modulators require large and power-consuming electrical driver amplifiers and have limited bandwidths ( $\sim 35$  GHz) (b). (c) Microscope image of the fabricated chip consisting of three Mach-Zehnder modulators with various microwave signal line widths and device lengths. The thin-film configuration allows for maximum field overlap and velocity matching between microwave and optics. Inset shows the cross-sectional schematic of the nanophotonic lithium-niobate modulator. (d) Normalized optical transmission of a 20-mm device as a function of the applied voltage, showing a low half-wave voltage of 1.4 V. The measured extinction ratio is 30 dB.

direct driving from CMOS electronics, and at the same time with bandwidths up to 100 GHz. Our modulators benefit from the superior electro-optic overlap in the monolithically integrated platform, matched velocity between light and microwave, and low optical and microwave propagation losses, simultaneously. Combining the low  $V_\pi$  and high bandwidth, we show high-speed data modulation with a modulation voltage as low as 60 mV, directly driven by a CMOS circuit. The excellent signal fidelity allows us to successfully demonstrate data transmission at 210 Gigabit per second (Gbit/s).

The integrated modulators operate in a travelling-wave Mach-Zehnder interferometer (MZI) configuration that utilizes highly-confined co-propagating microwave and optical fields with matched group velocities (Fig. 1). A 50:50 Y-junction splits the input light into two LN optical waveguides that form the arms of MZI. The optical waveguides run through the dielectric gaps of the Ground-Signal-Ground (GSG) coplanar microwave strip line (Fig. 1C). As a result, the microwave electric field has opposite signs across the two LN waveguides, thus inducing (via the Pockels effect) an optical phase delay on one arm and an optical phase advance on the other. This optical phase difference results in constructive/destructive interference and thereby an amplitude modulation of the output optical signal as the arms are recombined using another 50:50 Y-junction (Fig. 1D).

An important figure of merit for MZI modulators is the half-wave voltage ( $V_\pi$ ), defined as the voltage to induce a  $\pi$ -phase difference between the two modulator arms, changing the optical transmission from maximum to minimum. For a device with 20-mm long microwave strip line electrodes, we measure a low  $V_\pi$  of 1.4 V (Fig. 1D), which allows for the modulator to be directly driven by CMOS circuit. Importantly, our devices also feature a high optical power extinction ratio of  $\sim 30$  dB between on and off states (See Supplementary).

In the travelling-wave electrode configuration, longer microwave strip lines could be used to induce a larger optical phase shift thus reducing the half-wave voltage. However, this also degrades the electro-optic bandwidth due to exacerbated microwave-optical velocity mismatch and microwave loss. This contradicting requirement on electrode length results in the so-called voltage-bandwidth trade-off [9]. In traditional LN modulators, the large optical mode size requires the metal electrodes to be placed far from the optical waveguides, and very long electrodes are required to reach even a modest  $V_\pi$ . As a result, the voltage-bandwidth performance of these modulators is typically limited to  $\sim 3.5$  V and 35 GHz, requiring power-consuming electrical amplifiers to drive them (Fig. 1B) [9].

In contrast, the thin-film LN modulator can overcome this trade-off by maximizing the electro-optic overlap us-

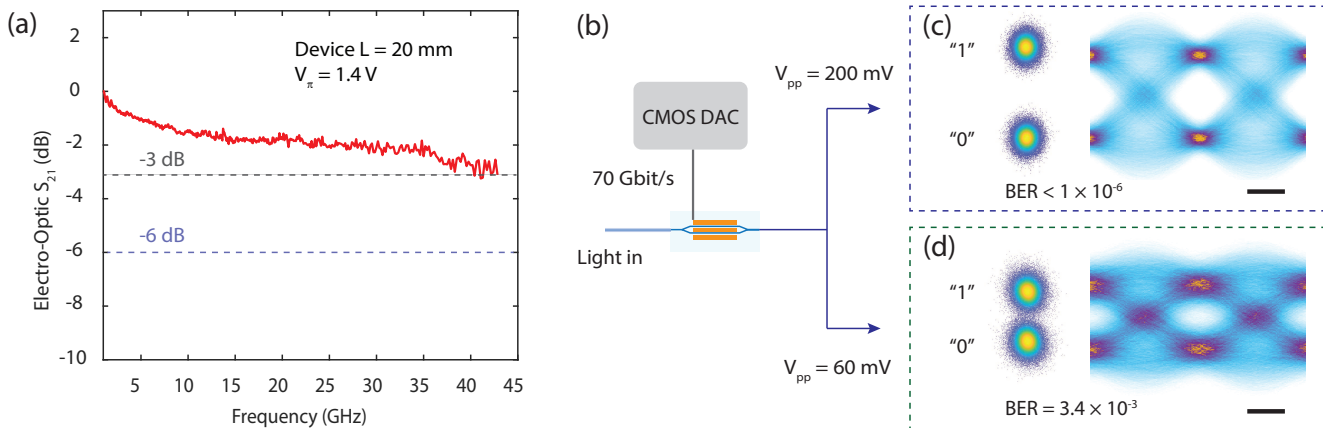


FIG. 2. **Directly CMOS-driven data transmission at 70 Gbit/s.** (a) Small-signal electro-optic response of a device with an active modulation length of 20 mm, showing a high 3-dB bandwidth of  $> 45$  GHz. (b) The device is used for data transmission experiments at 70-Gbit/s rate, directly driven by a CMOS circuit. Peak-to-peak voltage levels of 200 mV (top) and 60 mV (bottom) are used. (c-d) Measured constellation diagrams using a coherent receiver (left), as well as the reconstructed eye diagrams (right). At modulation voltages of 200 mV (c) and 60 mV (d), the measured bit-error ratios (BER) are  $< 1 \times 10^{-6}$  and  $3.4 \times 10^{-3}$ , respectively. The eye diagrams are obtained by up-sampling the received data for better visualization. Scale bars: 5 ps.

ing photonic structures with a sub-wavelength optical confinement [23, 24, 27]. Moreover, the microwave and optical group velocities can be engineered and matched by designing the LN/SiO<sub>2</sub>/Si-stack without sacrificing the electro-optic overlap (See Supplementary). As a result, our devices are dramatically shorter (ranging from 5 mm to 20 mm) than conventional counterparts, allowing for high electro-optic bandwidth while operating at CMOS-level  $V_{\pi}$  (Fig. 1A). Fig. 2A presents the measured small-signal electro-optic response of the 20-mm long device, showing a high 3-dB bandwidth of  $> 45$  GHz. Owing to our recent development in LN nanofabrication [26], the devices also possess ultra-low on-chip optical losses of  $< 0.5$  dB.

We use the low-voltage, high-bandwidth integrated modulators to demonstrate data modulation at 70 Gbit/s directly driven by a CMOS circuit (Fig. 2B-D). High-speed electrical signals are generated by a CMOS digital-to-analog conversion (DAC) circuit, and directly used to drive our modulator without an electrical amplifier. Figure 2C-D shows the measured constellation diagrams (left) from a coherent receiver, which recovers both in-phase (vertical) and quadrature (horizontal) components of the output optical field at each data-sampling time. Distinct constellations with less overlapping data points correspond to lower bit-error ratios (BER). The eye diagrams (Fig. 2C-D right) are generated by up-sampling the received digital data for better visualization. At a peak-to-peak drive voltage ( $V_{pp}$ ) of 200 mV, the modulated optical signal yields error-free performance within the  $1.1 \times 10^6$  captured signal bits, i.e.  $\text{BER} < 1 \times 10^{-6}$  (Fig. 2B top). In this case, the electrical energy dissipation within our modulator is 0.37 fJ/bit (See Supplementary). We note that the overall energy consumption

of the complete data transmission system is dominated by off-chip components, including CMOS DAC, laser, receiver setup and analog-to-digital converters (ADC). The system can also operate at a further reduced driving voltage of  $V_{pp} = 60$  mV, with a BER of  $3.4 \times 10^{-3}$  (Fig. 2B bottom). In this case the electrical energy dissipation of the modulator is further reduced to 37 aJ/bit.

The high electro-optic bandwidth and excellent signal fidelity of our modulator allow for data transmission at even higher rates, currently up to 210 Gbit/s. To achieve this, we amplify the electrical signals from the CMOS DAC to a  $V_{pp}$  of  $\sim 2.5$  V (Fig. 3A). We first test our modulator at an ultra-high symbol rate of 100 Gbaud (Fig. 3B) (29). The BER of  $7.8 \times 10^{-5}$  in this case is limited by distortion from the electrical source at high frequencies the electrical BER at 100 Gbaud without any electrical-to-optical-to-electrical conversion is  $3.6 \times 10^{-5}$  (See Supplementary). We then use multi-level modulation formats at 70 Gbaud to further increase the data rates. Using 4-amplitude shift keying (2 bits per symbol, 4-ASK), we can achieve a data transmission rate of 140 Gbit/s, with a low BER of  $2.1 \times 10^{-5}$ . In the case of 8-ASK (3 bits per symbol), the modulator transmits a total data rate of 210 Gbit/s. The measured BER of  $1.5 \times 10^{-2}$  is within the tolerance of forward error correction with a 20% overhead (tolerable  $\text{BER} = 1.9 \times 10^{-2}$ ). In the latter case, the electrical energy dissipation of our modulator is 14 fJ/bit (See Supplementary).

We show that the integrated LN platform offers dramatically improved overall performance (voltage, bandwidth and optical loss) over traditional LN modulators and other material platforms. By reducing the device lengths to 10 mm and 5 mm, we further expand the 3-dB electro-optic bandwidths to 80 GHz and 100 GHz

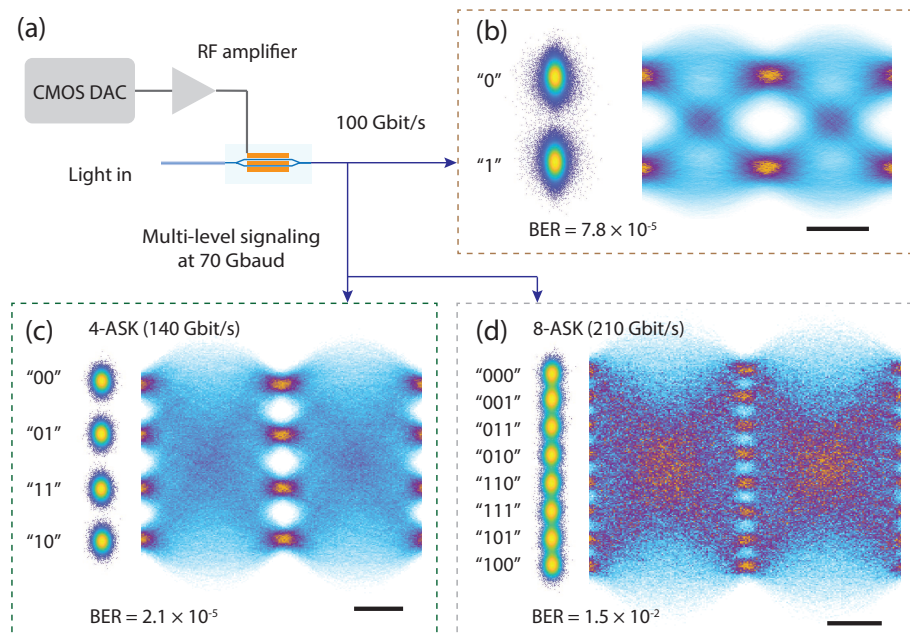


FIG. 3. **Ultra-high-speed data transmission at 100 Gbaud and 210 Gbit/s.** (a) Binary signals at an ultra-high symbol rate of 100 Gbaud, as well as multi-level signals at 70 Gbaud, are generated from a CMOS circuit and amplified to a peak-to-peak voltage of 2.5 V to drive the integrated modulator. (b) Constellation diagram and reconstructed eye diagram of data transmission at 100 Gbaud. The relatively high bit-error ratio (BER) of  $7.8 \times 10^{-5}$  is limited by the electrical signal quality at this ultrahigh speed. (c-d) Multi-level data modulation at a symbol rate of 70 Gbaud. The 4-level (c) and 8-level (d) amplitude-shift keying (ASK) enable even higher data transmission rates of 140 Gbit/s and 210 Gbit/s, respectively. The measured BERs are  $2.1 \times 10^{-5}$  and  $1.5 \times 10^{-2}$  respectively. Scale bars: 5 ps.

respectively (Fig. 4A-B). The electro-optic response at ultra-high frequencies up to 100 GHz are measured using an optical spectrum analyzer [28] (See Supplementary). The measured  $V_{\pi}$ s for these devices are 2.3 V and 4.4 V respectively. In comparison with commercial LN modulators and previously reported thin-film LN devices, our modulators show significantly better voltage-bandwidth performance, as is illustrated in Fig. 4C (See Supplementary for references). The ultra-high bandwidth of these modulators could allow for data operation beyond 200 Gbaud. Furthermore, unlike other high-speed modulator platforms where the active modulation regions can induce high optical propagation losses, the chip-scale integration of LN here allows for low optical loss and low  $V_{\pi}$ s at the same time (Figure 4D). Using even longer devices, we can potentially further reduce the  $V_{\pi}$  well below 1 V while maintaining an on-chip loss of  $< 1$  dB.

The results presented here show that the ultra-high-performance integrated LN modulators could become a key enabler for future high-bandwidth and low-power-consumption data communications. Combining the excellent signal fidelity with advanced in-phase/quadrature (I/Q) modulator design, a single integrated LN modulator can potentially transmit  $> 1$  Tb/s of data (e.g. 64-quadrature amplitude modulation (64-QAM) at 200

Gbaud). The small footprint and low voltage also allows for direct optoelectronic integration of switching components with coherent application-specific integrated circuits (ASIC) [2]. Furthermore, the low optical and microwave losses, linear electro-optic response, scalability and the ability to be integrated with other photonic components (e.g. filters and delay lines) could inspire a new generation of active integrated optoelectronic circuits, including large-scale GHz switching networks for quantum photonics [5], radio signal processing in the optical domain for microwave photonics [4], as well as self-aware optical networks [29], non-reciprocal devices [8] and topological photonic circuits [30].

The authors thank J. Khan, C. Reimer, S. Bogdanovic, L. Shao and B. Desiatov for fruitful discussions. This work is supported in part by National Science Foundation (NSF) (ECCS1609549, ECCS-1740296 E2CDA, and DMR-1231319), and by Harvard University Office of Technology Development (Physical Sciences and Engineering Accelerator Award). Device fabrication is performed at the Harvard University Center for Nanoscale Systems (CNS), a member of the National Nanotechnology Coordinated Infrastructure Network (NNCI), which is supported by the National Science Foundation under NSF ECCS award no. 1541959.

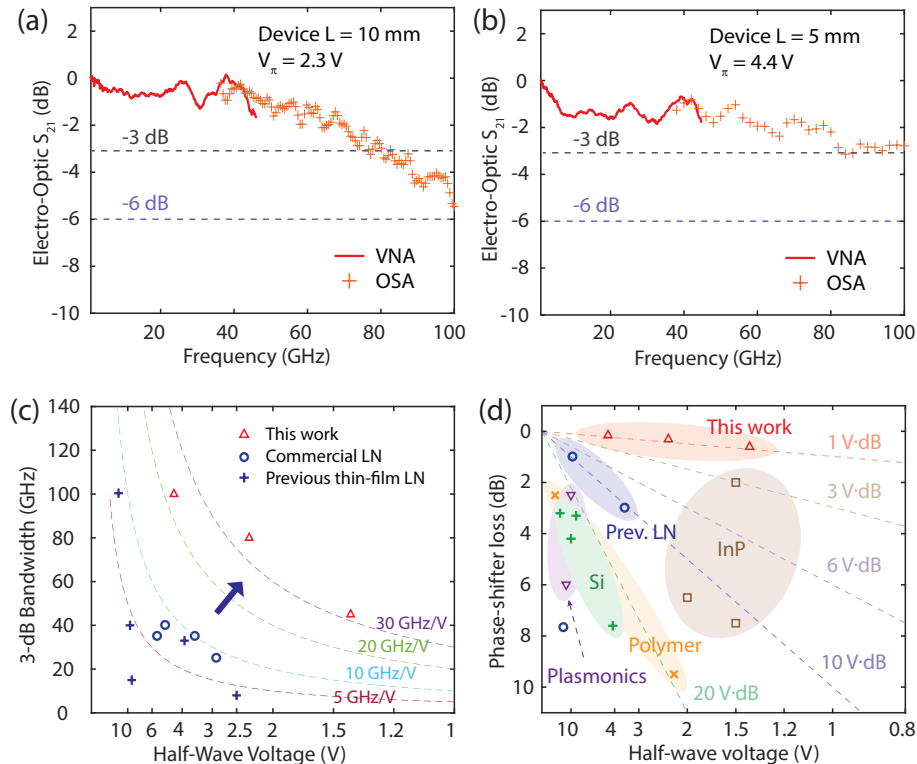


FIG. 4. **Towards ultimate modulator performance.** Electro-optic responses of a 10-mm (a) and a 5-mm (b) device, showing ultra-high 3-dB bandwidths of 80 GHz and 100 GHz, respectively. The low-frequency (red) and high-frequency (orange) measurements are performed using vector network analyzer (VNA) and optical spectrum analyzer (OSA), respectively. (c) Key modulator figure of merit ( $B/V_\pi$ , ratio between 3-dB electro-optic bandwidth  $B$  and half-wave voltage  $V_\pi$ ) comparison of this work, state-of-the-art commercial lithium-niobate modulators, and previous thin-film lithium-niobate modulators, showing dramatically higher bandwidths and lower half-wave voltages. The dotted lines correspond to constant values of  $B/V_\pi$ . The half-wave voltage is shown in inverse scale ( $1/V_\pi$ ) to better visualize  $B/V_\pi$ . (d) In comparison with other material platforms with  $B > 40$  GHz, our modulators show much lower  $V_\pi$  and on-chip optical loss at the same time. The optical losses in the active modulation regions are used for fair comparison between different platforms. Detailed references for the data shown in (c-d) can be found in Supplementary.

\* These authors contributed equally to this work

† loncar@seas.harvard.edu

- [1] G. T. Reed, G. Mashanovich, F. Y. Gardes, and D. J. Thomson, *Nat. Photonics* **4**, 518 (2010).
- [2] D. A. B. Miller, *J. Lightwave Technol.* **35**, 346 (2017).
- [3] T. M. Fortier, M. S. Kirchner, F. Quinlan, J. Taylor, J. C. Bergquist, T. Rosenband, N. Lemke, A. Ludlow, Y. Jiang, C. W. Oates, and S. A. Diddams, *Nat. Photonics* **5**, 425 (2011).
- [4] P. Ghelfi, F. Laghezza, F. Scotti, G. Serafino, A. Capria, S. Pinna, D. Onori, C. Porzi, M. Scaffardi, A. Malacarne, V. Vercesi, E. Lazzeri, F. Berizzi, and A. Bogoni, *Nature* **507**, 341 (2014).
- [5] J. L. Brien, *Science* **318**, 1567 (2007).
- [6] M. Kues, C. Reimer, P. Roztocky, L. R. Cortes, S. Sciara, B. Wetzal, Y. Zhang, A. Cino, S. T. Chu, B. E. Little, D. J. Moss, L. Caspani, J. Azaa, and R. Morandotti, *Nature* **546**, 622 (2017).
- [7] Z. Yu and S. Fan, *Nat. Photonics* **3**, 91 (2009).
- [8] L. D. Tzuang, K. Fang, P. Nussenzeig, S. Fan, and M. Lipson, *Nat. Photonics* **8**, 701 (2014).
- [9] E. L. Wooten, K. M. Kissa, A. Yi-Yan, E. J. Murphy, D. A. Lafaw, P. F. Hallemeier, D. Maack, D. V. Attanasio, D. J. Fritz, G. J. McBrien, and D. E. Bossi, *IEEE J. Sel. Top. Quant. Electron.* **6**, 69 (2000).
- [10] Q. Xu, B. Schmidt, S. Pradhan, and M. Lipson, *Nature* **435**, 325 (2005).
- [11] C. Sun, M. T. Wade, Y. Lee, J. S. Orcutt, L. Alloatti, M. S. Georgas, A. S. Waterman, J. M. Shainline, R. R. Avizienis, S. Lin, B. R. Moss, R. Kumar, F. Pavanello, A. H. Atabaki, H. M. Cook, A. J. Ou, J. C. Leu, Y.-H. Chen, K. Asanovi, R. J. Ram, M. A. Popovi, and V. M. Stojanovi, *Nature* **528**, 534 (2015).
- [12] Y. Ogiso, J. Ozaki, Y. Ueda, N. Kashio, N. Kikuchi, E. Yamada, H. Tanobe, S. Kanazawa, H. Yamazaki, Y. Ohiso, T. Fujii, and M. Kohtoku, *J. Lightwave Technol.* **35**, 1450 (2017).
- [13] M. Aoki, M. Suzuki, H. Sano, T. Kawano, T. Ido,

- T. Taniwatari, K. Uomi, and A. Takai, *IEEE J. Quant. Electron.* **29**, 2088 (1993).
- [14] S. Koeber, R. Palmer, M. Lauermaun, W. Heni, D. L. Elder, D. Korn, M. Woessner, L. Alloatti, S. Koenig, P. C. Schindler, H. Yu, W. Bogaerts, L. R. Dalton, W. Freude, J. Leuthold, and C. Koos, *Light Sci. Appl.* **4**, e255 (2015).
- [15] M. Lee, H. E. Katz, C. Erben, D. M. Gill, P. Gopalan, J. D. Heber, and D. J. McGee, *Science* **298**, 1401 (2002).
- [16] M. Ayata, Y. Fedoryshyn, W. Heni, B. Baeuerle, A. Josten, M. Zahner, U. Koch, Y. Salamin, C. Hoessbacher, C. Haffner, D. L. Elder, L. R. Dalton, and J. Leuthold, *Science* **358**, 630 (2017).
- [17] R. W. Boyd, *Nonlinear optics* (Academic press, 2003).
- [18] D. Janner, D. Tulli, M. Garca-Granda, M. Belmonte, and V. Pruneri, *Laser Photonics Rev.* **3**, 301 (2009).
- [19] R. V. Schmidt and I. P. Kaminow, *Applied Physics Letters* **25**, 458 (1974).
- [20] G. Poberaj, H. Hu, W. Sohler, and P. Gnter, *Laser Photonics Rev.* **6**, 488 (2012).
- [21] H. Liang, R. Luo, Y. He, H. Jiang, and Q. Lin, arXiv preprint arXiv:1706.08904 (2017).
- [22] J. Wang, F. Bo, S. Wan, W. Li, F. Gao, J. Li, G. Zhang, and J. Xu, *Optics Express* **23**, 23072 (2015).
- [23] C. Wang, M. Zhang, B. Stern, M. Lipson, and M. Lonar, *Opt. Express* **26**, 1547 (2018).
- [24] A. Rao, A. Patil, P. Rabiei, A. Honardoost, R. DeSalvo, A. Paoletta, and S. Fathpour, *Opt. Lett.* **41**, 5700 (2016).
- [25] L. Chen, Q. Xu, M. G. Wood, and R. M. Reano, *Optica* **1**, 112 (2014).
- [26] M. Zhang, C. Wang, R. Cheng, A. Shams-Ansari, and M. Lonar, *Optica* **4**, 1536 (2017).
- [27] S. Jin, L. Xu, H. Zhang, and Y. Li, *IEEE Photonics Technol. Lett.* **28**, 736 (2016).
- [28] X. Chen, S. Chandrasekhar, S. Randel, G. Raybon, A. Adamiecki, P. Pupalakakis, and P. J. Winzer, *J. Light-wave Technol.* **35**, 411 (2017).
- [29] D. A. B. Miller, *Science* **347**, 1423 (2015).
- [30] L. Yuan, M. Xiao, Q. Lin, and S. Fan, arXiv preprint arXiv:1710.01373 (2017).
- [31] X. Chen, S. Chandrasekhar, G. Raybon, P. Dong, B. Li, A. Adamiecki, and P. Winzer, in *2017 Optical Fiber Communications Conference and Exhibition (OFC)* (2017) p. Tu2H.7.
- [32] A. J. Mercante, P. Yao, S. Shi, G. Schneider, J. Murakowski, and D. W. Prather, *Optics Express* **24**, 15590 (2016).
- [33] P. O. Weigel, J. Zhao, K. Fang, H. Al-Rubaye, D. Trotter, D. Hood, J. Mudrick, C. Dallo, A. T. Pomerene, A. L. Starbuck, C. T. DeRose, A. L. Lentine, G. Rebeiz, and S. Mookherjea, arXiv:1803.10365 [physics] (2018), arXiv: 1803.10365.
- [34] P. Dong, X. Liu, S. Chandrasekhar, L. L. Buhl, R. Aroca, and Y. K. Chen, *IEEE Journal of Selected Topics in Quantum Electronics* **20**, 150 (2014).
- [35] D. J. Thomson, F. Y. Gardes, J. M. Fedeli, S. Zlatanovic, Y. Hu, B. P. P. Kuo, E. Myslivets, N. Alic, S. Radic, G. Z. Mashanovich, and G. T. Reed, *IEEE Photonics Technology Letters* **24**, 234 (2012).
- [36] M. Streshinsky, R. Ding, Y. Liu, A. Novack, Y. Yang, Y. Ma, X. Tu, E. K. S. Chee, A. E.-J. Lim, P. G.-Q. Lo, T. Baehr-Jones, and M. Hochberg, *Optics Express* **21**, 30350 (2013).
- [37] S. S. Azadeh, F. Merget, S. Romero-Garca, A. Moscoso-Mrtir, N. von den Driesch, J. Mller, S. Mantl, D. Buca, and J. Witzens, *Optics Express* **23**, 23526 (2015).
- [38] E. Rouvalis, in *IEEE Compound Semiconductor Integrated Circuit Symposium (CSICS)* (2015) pp. 1–4.
- [39] G. Letal, K. Prosyk, R. Millett, D. Macquistan, S. Paquet, O. Thibault-Maheu, J. F. Gagn, P. L. Fortin, R. Dowlatshahi, B. Rioux, T. SpringThorpe, M. Hisko, R. Ma, and I. Woods, in *2015 Optical Fiber Communications Conference and Exhibition (OFC)* (2015) pp. 1–3.
- [40] S. Wolf, H. Zwickel, C. Kieninger, M. Lauermaun, W. Hartmann, Y. Kutuvantavida, W. Freude, S. Randel, and C. Koos, *Optics Express* **26**, 220 (2018).
- [41] L. Alloatti, R. Palmer, S. Diebold, K. P. Pahl, B. Chen, R. Dinu, M. Fournier, J.-M. Fedeli, T. Zwick, W. Freude, C. Koos, and J. Leuthold, *Light: Science & Applications* **3**, e173 (2014).
- [42] C. Haffner, W. Heni, Y. Fedoryshyn, J. Niegemann, A. Melikyan, D. L. Elder, B. Baeuerle, Y. Salamin, A. Josten, U. Koch, C. Hoessbacher, F. Ducry, L. Juchli, A. Emboras, D. Hillerkuss, M. Kohl, L. R. Dalton, C. Hafner, and J. Leuthold, *Nat Photon* **9**, 525 (2015).

## Supplemental Information

### I. MATERIALS AND METHODS

#### A. Device fabrication procedure

Devices are fabricated from a commercial x-cut lithium-niobate-on-insulator (LNOI) wafer (NANOLN), where a 600-nm device layer sits on top of a SiO<sub>2</sub>/Si-stack substrate. Electron-beam lithography (EBL) and Ar<sup>+</sup> ion based reactive ion etching (RIE) are performed to define optical waveguides and Mach-Zehnder interferometers in thin-film lithium niobate (LN), using a similar process as described in [S26]. A 1.5- $\mu$ m-thick PMMA EBL resist is spun coated and exposed using a second EBL with alignment, to define the microwave transmission line patterns. The PMMA resist is used for a lift-off process to produce the 500-nm-thick gold stripe lines. The structures are then cladded by an 800-nm-thick SiO<sub>2</sub> layer using plasma-enhanced chemical vapor deposition (PECVD). Finally, the chip edges are diced and polished to improve the fiber-chip coupling.

#### B. Electro-optic characterization and bandwidth measurement

Electro-optic characterization is performed in the telecom C-band using a tunable-wavelength laser source (Santec TSL-510). A 3-paddle polarization controller is used to ensure transverse-electric (TE) mode excitation. Light is butt-coupled into and out from the chip under test using tapered lensed fibers, with a coupling loss of  $\sim 5$  dB/facet. For half-wave voltage ( $V_\pi$ ) measurement, a triangular voltage signal ( $V_{pp} = 5$  V) at 75 kHz is used to drive the modulator while the optical transmission signal is monitored in real time. A pair of high-speed microwave probes (GGB) is used to deliver the modulation signal to the input port of the transmission line, and to terminate the transmission line with a 50- $\Omega$  load. The electro-optic response below 45 GHz is measured using a vector network analyzer (VNA) in a similar setup as that used in [S28].

The electro-optic response from 35 GHz to 100 GHz is tested using an optical spectrum analyzer (OSA), as is shown in Fig. S1A [S28]. A sinusoidal signal ( $f_i$ ) from a high-speed synthesizer (up to 50 GHz) is used to drive a commercial LN Mach-Zehnder modulator (MZM), which has a 3-dB bandwidth of  $\sim 35$  GHz and possesses finite response at 50 GHz. The modulator is biased at the transmission null point to suppress the carrier frequency, resulting in an output optical signal with two sidebands separated by twice the input frequency ( $2 f_i$ ). A 100-GHz photodetector is used to beat the two sidebands and generate a microwave signal up to 100 GHz, which is subsequently used to drive the modulator under test. The modulator optical response is measured by monitoring the sideband power in the OSA. We calibrate the synthesizer output power, the commercial MZM electro-optic response, and the 100-GHz photodetector response over the frequency range of interest to ensure an accurate characterization of our devices. Note that the actual measurement is performed using a pair of 67-GHz probes (one for RF signal modulation and the other for 50- $\Omega$  termination). Calibration of the frequency response of the probes are not embedded due to the lack of manufacturer data. Therefore, the bandwidth reported here is a lower bound for our devices.

#### C. High-speed data transmission test

Figure S1B shows the measurement setup for high-speed data modulation test. Electrical signals up to 70 Gbaud are directly generated from a CMOS digital-to-analog conversion (DAC) circuit (Socionext OOLA DAC, 3-dB analog bandwidth = 15 GHz, 13-dB analog bandwidth = 35 GHz). The electrical signals from the DAC has a peak-to-peak voltage of  $\sim 0.2$  V, and can be further amplified or attenuated before being used to drive the modulator under test. The modulator is biased at the transmission null point to allow coherent detection. The output optical signal is mixed with a local oscillator in an optical hybrid, and sent into a single-polarization coherent receiver with a pair of balanced 45-GHz photodetectors to extract the in-phase and quadrature components of the modulated light field. Digitized data are collected using an 80-GSa/s real-time oscilloscope with an analog bandwidth of 63 GHz (Keysight DSOZ634A). The collected data are post-processed using digital signal processing (DSP) to equalize the optical channel response (laser phase drifts etc.), and to generate the constellation diagrams. The eye diagrams are plotted by up-sampling the real-part of the recovered constellations for better visualization. For optical signal-to-noise ratio (OSNR) measurement, the modulator output optical signal is attenuated to different levels to reduce the OSNR, before being amplified again and sent to the coherent receiver (attenuator and amplifier not shown in Fig. S1B). For symbol rates at 100 Gbaud, the electrical signal is generated by up-conversion and interleaving two 35-GHz electrical signals using a similar circuit as is described in [S31].

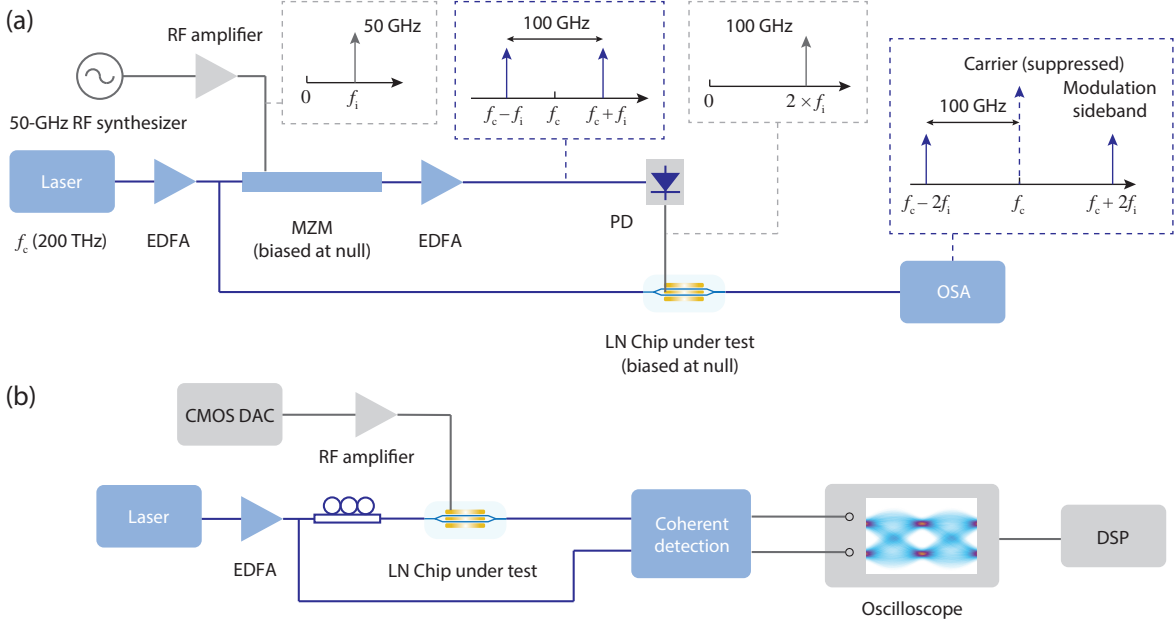


FIG. S1. **High-speed measurement setups.** (a) Electro-optic bandwidth measurement up to 100 GHz. A sinusoidal signal ( $f_i$ ) from a 50-GHz synthesizer is used to drive a MZM, which is biased at the transmission null point to suppress the carrier tone. The resulting output optical signal has two sidebands separated by twice the input frequency ( $2f_i$ ), and is sent to A 100-GHz PD. The PD beats the two sidebands and generate a microwave signal up to 100 GHz, which is used to drive the modulator under test. The modulator electro-optical responses at different frequencies are measured by monitoring the sideband power in the OSA. (b) High-speed data modulation setup. Electrical signals from a CMOS DAC is amplified to a peak-to-peak voltage ( $V_{pp}$ ) of 2.5 V, and used to drive the modulator under test. The output optical signal from the modulator is mixed with a local oscillator in an optical hybrid and sent to a coherent receiver with a pair of balanced PD. Real-time electrical signals are recorded using a 63-GHz oscilloscope. For direct CMOS driving test, the RF amplifier is bypassed. DAC, digital-to-analog converter; EDFA, erbium-doped fiber amplifier; MZM, Mach-Zehnder modulator (commercial); OSA, optical spectrum amplifier.

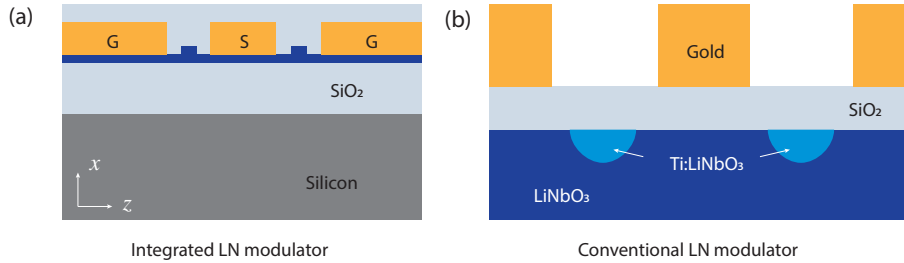


FIG. S2. **Cross-sectional schematics of integrated and conventional lithium niobate modulators.** (a) Thin-film modulator has the oxide layer underneath the device layer, so that velocity matching can be achieved while the maximum electro-optic efficiency is maintained. (b) Conventional modulator also uses a buffer oxide layer for velocity matching, but on top of lithium niobate which further compromises the electro-optic overlap.

## II. CROSS-SECTION SCHEMATICS OF INTEGRATED AND CONVENTIONAL LN MODULATOR

Figure S2 shows the cross-sectional schematics of the integrated LN modulator (a) and the conventional LN modulator (b). Due to the high optical confinement in thin-film LN platform, the metal electrodes can be placed close to each other, resulting in much higher electro-optic efficiency. Moreover, the  $\text{SiO}_2/\text{Si}$ -stack substrate can be independently designed as a microwave dielectric to realize optimal microwave-optical group velocity matching without sacrificing electro-optic overlap. In contrast, the already suboptimal electro-optic efficiency in conventional LN modulators is

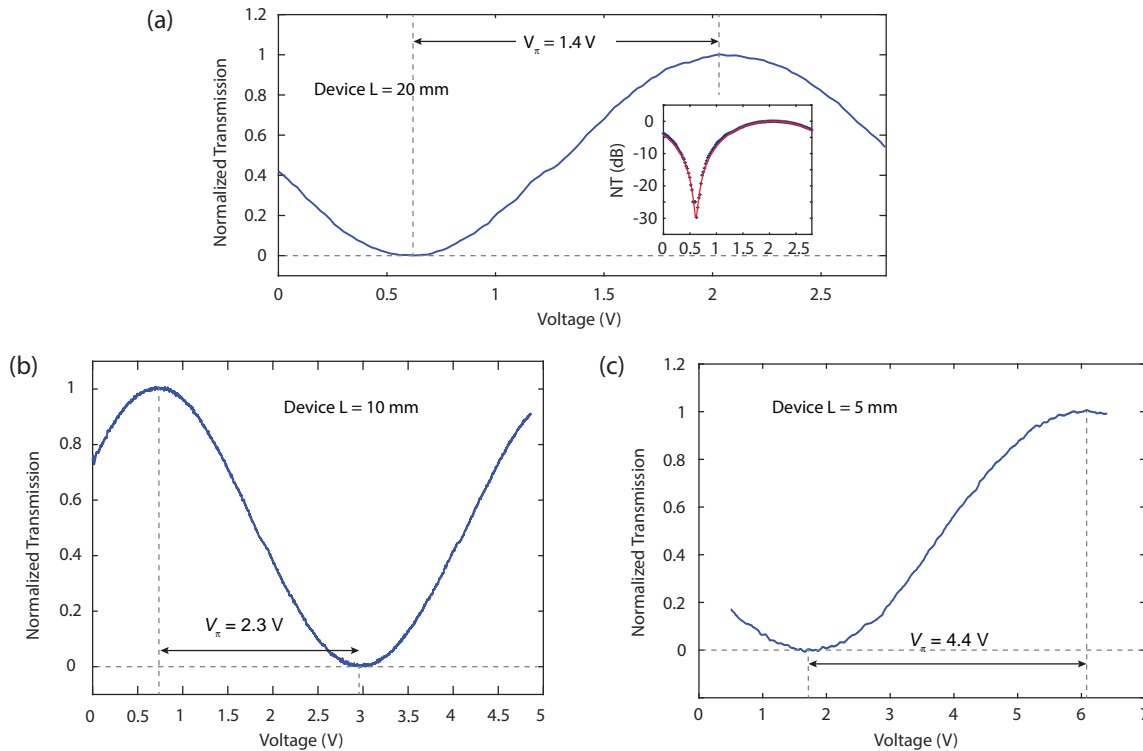


FIG. S3. **Half-wave voltages of devices with different active lengths.** Normalized optical transmission of the 20-mm (a), 10-mm (b) and 5-mm (c) device as a function of the applied voltage, showing half-wave voltage of 1.4 V (a), 2.3 V (b) and 4.4 V (c). The inset of (a) shows the measured transmission in logarithmic scale, revealing an extinction ratio of 30 dB.

further reduced by the buffer  $\text{SiO}_2$  layer in order to overcome large group velocity mismatch between microwave and optical signals. The latter is due to large discrepancy between the dielectric constants of lithium niobate at microwave ( $\epsilon_{\text{RF}} = 28$ ) and optical ( $\epsilon_{\text{opt}} = 5$ ) frequencies.

### III. MICROWAVE TRANSMISSION LINE

The RF and optical simulations are performed using Finite Element Method (FEM, COMSOL Multiphysics). We design the waveguide width, ridge height and metal gap to achieve the optimum electro-optic overlap with negligible optical loss inside the waveguides. We design the coplanar waveguide signal line width and the substrate  $\text{SiO}_2$  thickness to achieve group velocity matching between RF and optics, and to have an impedance near  $50 \Omega$ .

### IV. DEVICE EXTINCTION RATIO

The inset of Fig. S3A shows the optical transmission as a function of applied voltage in logarithmic scale, for the modulator with an active device length of 20 mm. The measured device extinction ratio is 30 dB.

### V. HALF-WAVE VOLTAGES OF THE 10-MM AND 5-MM LONG DEVICES

Figure S3B-C shows the half-wave voltage measurements for the 10-mm and 5-mm devices. The measured  $V_\pi$ s are 2.3 V and 4.4 V, corresponding to voltage-length products of 2.3 V-cm and 2.2 V-cm, respectively.

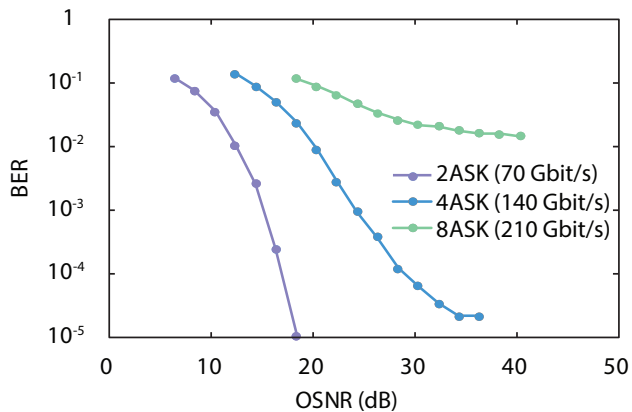


FIG. S4. **Optical signal-to-noise ratio measurements.** Bit-error rates (BER) versus optical signal-to-noise ratio (OSNR) for the three modulation schemes at 70 Gbaud.

Type	Half-wave voltage	E/O bandwidth	Reference
Thin-film LN	4 V	33 GHz	[S24]
Thin-film LN	9.4 V	40 GHz	[S32]
Thin-film LN	9 V	15 GHz	[S23]
Thin-film LN	2.5 V	8 GHz	[S27]
Thin-film LN	13 V	100 GHz	[S33]
Commercial LN	3.5 V	35 GHz	Fujitsu
Commercial LN	4.5-4.9 V	30-40 GHz	EO Space
Commercial LN	2.9-3.3 V	20-25 GHz	EO Space
Commercial LN	5.5 V	35 GHz	Thorlabs

TABLE S1. **Modulator figure of merit comparison.** Detailed half-wave voltages and electro-optic bandwidths of commercial LN modulators and previously demonstrated thin-film LN modulators are listed.

## VI. OPTICAL SIGNAL-TO-NOISE RATIO (OSNR) MEASUREMENT

We measure the relationship between the bit-error ratios (BER) and the optical signal-to-noise ratio (OSNR) for three different modulation schemes at a symbol rate of 70 Gbaud (Fig. S4). The results show the performance of our modulators in practical settings where external noise sources are present. For example, at a BER level of  $2 \times 10^{-2}$ , the OSNR is  $\sim 3$  dB away from theoretical value. This implementation penalty comes from various sources including the nonlinear response of the electronic driving circuit at high speeds.

## VII. MODULATOR FIGURE OF MERIT COMPARISON

Table S1 lists the detailed numbers ( $V_{\pi}$  values and electro-optic bandwidths) and references of commercial LN modulators and previously demonstrated thin-film LN modulators used in Fig. S4C. Table S2 lists the on-chip propagation losses and V values of high-speed ( $> 40$  GHz) modulators realized in other material platforms. These numbers are used in Fig. S4D.

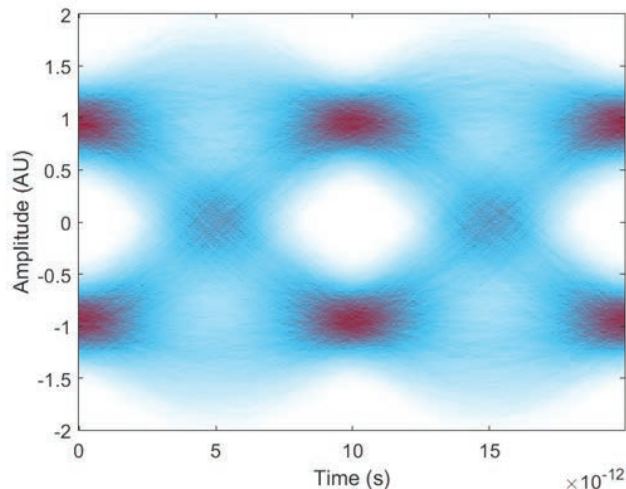


FIG. S5. **Electrical eye diagram at 100 Gbaud.** The measured electrical BER is  $3.6 \times 10^{-5}$ , limited by the signal distortion from the electronic circuit.

### VIII. ELECTRICAL EYE DIAGRAM AT 100 GBAUD

Figure S5 shows the electrical eye diagram at 100 Gbaud, with a BER of  $3.6 \times 10^{-5}$ , limited by the signal distortion from the electronic circuit. The high electrical BER resulted in the relatively high BER in the optically modulated signal at 100 Gbaud.

### IX. ENERGY CONSUMPTION CALCULATION

Since our modulator uses a transmission line configuration with a 50- load, the electrical energy dissipated in the modulator can be estimated as  $W_e = V_{\text{rms}}^2 / (BR)$ , where  $V_{\text{rms}}$  is the root-mean-square drive voltage,  $B$  is the bit-rate and  $R$  is the driver impedance [S14].

For the direct CMOS modulation at 70 Gbit/s (Fig. S2C-D), The electrical root-mean-square voltage  $V_{\text{rms}} = 36$  mV, resulting in a low electrical energy consumption of 0.37 fJ/bit. For the 210 Gbit/s data modulation test in Fig. S3D, the electrical  $V_{\text{rms}}$  is 360 mV, resulting in an electrical energy consumption of 14 fJ/bit. The energy consumption of the entire data transmission system also includes the power consumption of CMOS DAC, laser, optical amplifiers and analog-to-digital converter.

Type	Half-wave voltage	On-chip loss	Reference
Thin-film LN	4 V	N/A	[S24]
Thin-film LN	9.4 V	1 dB	[S32]
Thin-film LN	9 V	15 GHz	[S23]
Thin-film LN	13 V	7.8 dB	[S33]
Commercial LN	3.5 V	3 dB	[S9]
Silicon	10 V	4.2 dB	[S34]
Silicon	16 V	3.2 dB	[S35]
Silicon	8.5 V	3.3 dB	[S36]
Silicon	4.1 V	7.6 dB	[S37]
Indium Phosphide	2 V	6.5 dB	[S38]
Indium Phosphide	16 V	3.2 dB	[S39]
Indium Phosphide	8.5 V	3.3 dB	[S12]
Polymer	2.2 V	9.5 dB	[S40]
Polymer	22 V	2.5 dB	[S41]
Plasmonics	12 V	6 dB	[S16]
Plasmonics	10 V	2.5 dB	[S42]

TABLE S2. **Comparison of optical losses and half-wave voltages in different platforms.** Detailed on-chip optical propagation losses and half-wave voltages of previous lithium-niobate (LN) modulators, as well as modulators based on silicon (Si), indium phosphide (InP), polymers and plasmonics with  $> 40$  GHz bandwidth, are listed.